UC San Diego
UC San Diego Previously Published Works

Title
Development of a UiO-Type Thin Film Electrocatalysis Platform with Redox-Active Linkers

Permalink
https://escholarship.org/uc/item/08v5097h

Journal
Journal of the American Chemical Society, 140(8)

ISSN
0002-7863

Authors
Johnson, Ben A
Bhunia, Asamanjoy
Fei, Honghan
et al.

Publication Date
2018-02-28

DOI
10.1021/jacs.7b13077

Peer reviewed

Development of a UiO-type thin film electrocatalysis platform with redox active linkers

Ben A. Johnson[a], **Asamanjoy Bhunia**[a], **Honghan Fei**[b,†], **Seth M. Cohen**[b], and **Sascha Ott**[*,a]

[a]Department of Chemistry Ångström Laboratory, Uppsala University Box 523, 75120 Uppsala (Sweden)

[b]Department of Chemistry and Biochemistry, University of California, La Jolla, San Diego, CA, 92023-0358, USA

Abstract

Metal organic frameworks (MOFs) as electrocatalysis scaffolds are appealing due to the large concentration of catalytic units that can be assembled in three dimensions. To harness the full potential of these materials, charge transport to the redox-catalysts within the MOF has to be ensured. Herein, we report the first electroactive MOF with the UiO/PIZOF topology (**Zr(dcphOH-NDI)**), *i.e.* one of the most widely used MOFs for catalyst incorporation, by using redox-active naphthalene diimide-based linkers (**dcphOH-NDI**). Hydroxyl groups were included on the **dcphOH-NDI** linker to facilitate proton transport through the material. Potentiometric titrations of **Zr(dcphOH-NDI)** show the proton responsive behavior via the –OH groups on the linkers and the bridging Zr-μ_3-OH of the secondary building units with pK_a values of 6.10 and 3.45, respectively. When grown directly onto transparent conductive fluorine-doped tin oxide (FTO), 1 μm thin films of **Zr(dcphOH-NDI)@FTO** could be achieved. **Zr(dcphOH-NDI)@FTO** displays reversible electrochromic behavior as a result of the sequential one-electron reductions of the redox-active NDI linkers. Importantly, 97% of the NDI sites are electrochemically active at applied potentials. Charge propagation through the thin film proceeds through a linker-to-linker hopping mechanism that is charge-balanced by electrolyte transport, giving rise to cyclic voltammograms of the thin films that show characteristics of a diffusion-controlled process. The equivalent diffusion coefficient, D_e, that contains contributions from both phenomena was measured directly by UV/Vis spectroelectrochemistry. Using KPF$_6$ as electrolyte, D_e was determined to D_e(KPF$_6$) = 5.4±1.1x10^{-11} cm^2 s^{-1}, while an increase in counter cation size to *n*-Bu$_4$N$^+$ led to a significant decrease of D_e by about one order of magnitude (D_e(*n*-Bu$_4$NPF$_6$) = 4.0±2.5x10^{-12} cm^2 s^{-1}).

[*]**Corresponding Author**: sascha.ott@kemi.uu.se.
[†]**Present Addresses**
Shanghai Key Laboratory of Chemical Assessment and Sustainability, School of Chemical Science and Engineering, Tongji University, Shanghai 200092, P.R. China.

Introduction

Metal-organic frameworks (MOFs) are a class of porous, crystalline materials made from polydentate organic linkers and inorganic metal nodes, so-called secondary binding units (SBUs).[1–3] In some cases, the organic linkers can be functionalized using postsynthetic modification (PSM),[4–5] postsynthetic exchange (PSE),[6] or via direct solvothermal synthesis[7] to incorporate catalytic units into the framework. Linkers constructed from molecular transition metal complexes[8–14] or open coordination sites at the SBUs[15–16] often serve as catalytic centers. The resulting materials exhibit many appealing properties for electrocatalysis applications,[17–18] such as permanent porosity that facilitates fast substrate diffusion, and site isolation of molecular catalysts inside the framework that inhibits bimolecular decomposition pathways. Moreover, MOFs provide exceptionally high surface areas with potential catalyst loadings that are orders of magnitude higher than those of corresponding monolayers on electrode surfaces. However, the potential of molecular redox catalysis in MOFs has been exploited only sporadically, a shortcoming that is due, in part, to the fact that MOFs are traditionally composed of redox-inactive organic linkers and metal clusters (e.g. d^0 Zr^{IV}, d^{10} Zn^{II}) that result in poor charge transport to the MOF-embedded catalysts.[19–20] As a consequence, the realization of effective electrocatalytic MOFs has remained a challenge.

MOF architectures that exhibit electroactive behavior or high conductivities typically are constructed from specialized linkers and have confined structures that enhance conduction through the framework. Recent reports of conducting 3D MOFs[21–22] utilize either through-space charge transport with aromatic π-stacked linkers,[23–24] through-bond charge transport via covalent linkages of metal-sulfur bonds (-M-S-) in semi-infinite chains,[25] or induced charge transport by guest molecules inserted between the SBUs.[26–27] These materials exhibit high conductivities ($10^{-7} - 10^{-3}$ S cm^{-1}),[21] but are limited in terms of porosity and chemical stability, which are crucial for catalysis.[17] Thus, reports of electrocatalysis in MOFs are limited to primarily porphyrin-based frameworks[8–11] or 2-D metal-organic layers[28–29] where the linkers serve dual roles as charge transport mediators and catalysts. Unfortunately, all of these materials have limited options for postsynthetic modification, which makes catalytic functionalization and tuning of these frameworks a significant challenge.

Conversely, highly stable, porous, and modular frameworks, like the UiO series (UiO = University of Oslo) of MOFs[30–31], make excellent vehicles in which to immobilize molecular catalysts. They typically exhibit excellent thermal[30] and chemical stability[32–33] even under catalytic conditions (i.e. under irradiation,[7, 12–13] at high and low pH, and at applied oxidative or reductive potentials).[34–35] In addition, the linkers can be easily exchanged or appended with catalytic units by postsynthetic methods.[36] In particular, the mild conditions required for PSE in MOFs with UiO connectivity are advantageous when the catalyst is not compatible with solvothermal conditions[37–38] or when incorporating catalysts into MOF thin films.[34, 39] Despite of all these advantages, the suitability of UiO-type MOFs as electrocatalysis platforms is currently limited because the Zr-based SBUs, as well as their phenyl carboxylate linkers, are redox-inactive within a reasonable potential window. Even when doped with an electroactive transition metal complex, they are

essentially non-conducting.38 UiO-type MOFs have been used in numerous catalytic applications, but to date none feature redox active organic linkers, which could be utilized for charge transport to catalytic sites during electrocatalysis.

Herein, we report an electroactive MOF, which combines the attractive properties of the UiO structure type, *i.e.* high surface area, porosity, chemical stability, and facile PSE, with charge transport pathways at the operating potential of many proton reduction catalysts. Naphthalene diimide (NDI) was selected as the redox-active functional unit and was appended with carboxylic acid groups (**dcphOH-NDI**, Figure 1) for UiO-type MOF fabrication. The NDI moiety is a common electron-acceptor in organic photovoltaics, and n-type organic semiconductor,40–42 and features two one-electron reductions at potentials with sufficient driving force for electron transfer to common proton reduction catalysts. In addition, further proton responsive components (hydroxyl substitutents) were added to the design of the framework to enhance proton conductivity or allow for proton-coupled electron transfer (PCET) pathways43–44 during catalysis. Several MOFs utilizing NDI-type linkers have been reported with interesting optical and electrochemical properties;45–53 however, as described above, many suffer from low surface areas, minimal tunability, and limited stability. Installing the relatively large (length ~19 Å) NDI linker in a UiO-type framework overcomes these limitations and results in a new material, **Zr(dcphOH-NDI)** (Figure 1) with high stability, porosity, and charge transport properties needed for electrocatalysis. When grown on conducting substrates (fluorine-doped tin oxide, FTO), a redox active thin film cathode material is obtained (**Zr(dcphOH-NDI)@FTO**). In contrast to prior porphyrin-based MOFs, the concept proposed herein decouples the redox hopping pathways from the sites of catalysis. The framework reported here, **Zr(dcphOH-NDI)** and its corresponding thin film on FTO, is one of the first examples of a redox-active UiO-type MOF, which has the potential to be readily utilized for electrocatalysis.

Results & Discussion

Synthesis and Characterization

The carboxylate functionalized NDI-linker **dcphOH-NDI** was obtained by the condensation of 1,4,5,8-napthalenetetracarboxylic dianhydride and 4-amino-3-hydroxybenzoic acid in DMF. Addition of ZrCl$_4$ to **dcphOH-NDI** with acetic acid as a modulator in DMF under solvothermal conditions (120 °C) resulted in the new material, **Zr(dcphOH-NDI)**. Upon inspection of the PXRD pattern, it is clear that this material is highly crystalline (Figure 2a). SEM images reveal the bulk microcrystalline powder to consist of intergrown octahedral shaped crystallites ~2 μm in length (Figure 2b). ZrMOFs with linear carboxylate ligands generally assume a typical topology containing Zr$_6$O$_4$(OH)$_4$ clusters connected by 12 linkers, characteristic of the UiO series. In this case, the PXRD pattern closely resembles the pattern simulated from the crystal structure of a recently reported UiO-66 analogue Zr-MOF with a two-fold interpenetrated structure (Zr-L$_6$; L$_6$ = 4,4′-[1,4-naphthalene-bis(ethyne-2,1-diyl)]-dibenzoate),54 containing naphthalene-based linkers of approximately the same size (length ~19 Å) (Figure S1). MOFs synthesized with extended linkers often result in instability, such as pore collapse upon solvent removal. Behrens and co-workers have recently introduced a highly-stable class of porous interpenetrated Zr-organic frameworks

(PIZOFs) with extended linkers.[55–56] PIZOFs contain SBUs with the same structure and connectivity as in UiO MOFs ($Zr_6O_4(OH)_4$ nodes with twelve-fold connectivity); however, the framework comprises two independent interpenetrating UiO networks. Additionally, the frameworks were found to be stable under ambient conditions as well as towards hydrolysis.[55] Examples of PIZOF analogs in the literature have shown their suitability for PSM[57–58] and potential for catalytic applications.[59–60] A comparison of the PXRD patterns, establishes that the structure of **Zr(dcphOH-NDI)** adopts UiO/PIZOF-connectivity with $Zr_6O_4(OH)_4$ nodes and two-fold interpenetration (i.e. PIZOF analog). Stability tests were performed by incubating the as-synthesized material in organic solvent (DMF), H_2O, and under ambient conditions in air for several days (Figure S2). Identical PXRD patterns were obtained before and after exposure to these conditions, which confirms the stability of framework. The incorporation of the NDI-linker inside the framework was probed by FTIR-ATR, where the bulk powder **Zr(dcphOH-NDI)** exhibits vibrational bands similar to the free ligand, although shifted slightly due to coordination with the Lewis acidic Zr^{4+} metal centers (Figure 2c and Figure S3).[13] Notably the C=O stretches occur between 1700-1600 cm^{-1} and a broad –OH stretching band is observed centered around ~3175 cm^{-1}. Additionally, ^{1}H NMR confirmed the presence of the NDI linker in the framework. After digesting **Zr(dcphOH-NDI)** with HF, peaks at chemical shifts matching **dcphOH-NDI** (Figure S4) were observed. Thermogravimetric analysis (TGA) measurements (Figure 2d) show an initial mass loss for **Zr(dcphOH-NDI)** at 100–200 °C, which is most likely due to removal of guest solvent molecules (DMF, etc…) from the framework. The material begins to decompose at ~400-450°C as evidenced by the large mass loss in that range.

N_2 sorption analysis showed **Zr(dcphOH-NDI)** to have a high degree of porosity and resulted in a Brunauer-Emmet-Teller (BET) surface area of 1531 $m^2 g^{-1}$ with a total pore volume (V_T) of 1.53 $cm^3 g^{-1}$ after degassing under dynamic vacuum at 85 °C (Figure 3a). These values are in accordance with typical PIZOFs that have large internal diameters (19 Å), resulting in BET surface areas on the order of 1250 $m^2 g^{-1}$.[55] Type-IV isotherms were observed for **Zr(dcphOH-NDI)** with a hysteresis loop characteristic of hierarchically structured micro-mesoporous materials. A recent example of a PCN-160 derivative, in which a hierarchical pore structure was achieved by missing linker defects introduced via linker labialization, displays type-IV isotherms with hysteresis.[61] This behavior was assigned to the presence of both micropores and mesopores. Similar results were also obtained for a series of hierarchically structured polyMOFs, which also show a hysteresis loop as a result of an interlaced framework structure.[62–63] Furthermore, **Zr(dcphOH-NDI)** exhibits pore sizes of ~13 Å in the microporous range as well as a low portion of mesopores, which were observed around 25 Å and 70 Å (Figure 3b). Thus, in the present case, it is likely that a combination of missing linker defects and the interpenetrated framework topology of **Zr(dcphOH-NDI)** produces the hierarchical structure observed in the isotherms and pore size distribution. The PXRD pattern before and after the gas sorption measurement was unchanged (Figure S5), indicating that the material retains its crystallinity and structural integrity even upon desolvation. Based on previous reports, small pore sizes and relatively low porosities have the potential to be limiting under catalytic conditions,[7, 12, 20, 64–66] as this obstructs the diffusion of substrates, products, and redox-mediators (counter-ions,

oxidants, or reductants). The high surface area and large pore size of **Zr(dcphOH-NDI)** is thus advantageous for catalytic applications where large open channels are required.

Protonation Behavior

Managing the transfer of multiple protons during redox reactions is essential for efficient catalysis. In analogy to natural enzymatic systems, the local environment and secondary coordination sphere around the catalytic active sites have profound influences on the reactivity and observed rates of catalytic reactions. For example, numerous reports have found that local hydroxyl groups near the binding site of a Fe-porphyrin-based CO_2 reduction catalyst greatly enhance the TOF during electrocatalysis.[67–68] MOFs present a unique opportunity to incorporate proton-responsive functionalities near the catalyst active sites within the framework. Several proton conductive MOFs have been reported for catalytic applications, including a NU-1000 film composed of MOF nanorods grown on a Ni-S catalyst film for electrocatalytic proton reduction.[69] The Zr-OH and Zr-OH$_2$ terminal groups on the NU-1000 SBUs assist in the proton transport to the catalyst on the surface of the electrode, which decreases the overpotential by 200 mV. In another example, Morris *et al.*[11] reported a Ni-metallated PCN-224 MOF thin-film with porphyrin linkers for water oxidation, where they proposed the Zr-oxo nodes act as proton acceptors under operating conditions at pH = 7, where the corresponding homogeneous complex is catalytically inactive due to the lack of sufficient Brønsted base.

This prompted us to examine the possibility of proton-responsive behavior in **Zr(dcphOH-NDI)** at either the Zr-nodes or the hydroxyl groups on the linker (Figure 1). Hupp and co-workers[70] recently developed an effective method to gauge the pK_a values using potentiometric titrations of terminal –OH and –OH$_2$ on the SBUs of various Zr-MOFs as well as that of defect sites within the framework. Following this procedure, the acid-base titration curve for **Zr(dcphOH-NDI)** is shown in Figure 4. Two equivalence points can be observed that correspond to pKa values of 3.45 ± 0.02 and 6.10 ± 0.05, which were assigned to the Zr-μ_3-OH and NDI-OH protons of the SBU and linker, respectively. The first pK_a value matches well with the reported pK_a for the bridging Zr-μ_3-OH proton of UiO-66 (pK_a = 3.52) and UiO-67 (pK_a = 3.44),[70] while the second pK_a value was assigned based on the titration curve of the free ligand in solution, which yielded a pK_a for the hydroxyl proton of 6.27 (Figure S6).[70] The PXRD pattern of the material after the titration is unchanged from before (Figure S7), indicating the framework is stable. It is clear from these experiments, **Zr(dcphOH-NDI)** exhibits proton-responsive behavior at both the Zr-SBUs and the hydroxyl-functionalized linker over a pH range of ~3.5-6.10. In this pH range, there would be both proton acceptor (SBUs) and proton donor units (linkers) present, which could be beneficial for proton transport under operating conditions in electrocatalytic applications.

Thin Film Characterization

To explore the electrochemical and optical properties of this new material, thin films of **Zr(dcphOH-NDI)** were grown on transparent conducting substrates. Thus, a self-assembled monolayer (SAM) of the NDI linker on FTO (**SAM@FTO**) was formed by soaking a FTO slide in a 1 mM solution of **dcphOH-NDI** in DMF for 18 h. Decreasing the amount of ZrCl$_4$ and **dcphOH-NDI** used in the reaction as compared to the bulk solvothermal synthesis

resulted in thin films of **Zr(dcphOH-NDI)@FTO**. Both PXRD (Figure 5a) and SEM (Figure 5b) confirmed the formation of the MOF thin film on FTO. The PXRD pattern is consistent with that of the bulk powder with minor changes in the intensity of some reflections, indicating a degree of orientation of the crystallites when grown on FTO. SEM images revealed the film is uniform and composed of interpenetrated crystallites in a ~1 μm thick layer (Figure S8). The SAM-modified FTO and **Zr(dcphOH-NDI)@FTO** were also characterized by XPS (Figure 5c,d). Absorption of the monolayer was confirmed by the N1s peak observed at a binding energy of 399.9 eV, arising from the NDI core of **dcphOH-NDI.**[71] The spectra of **Zr(dcphOH-NDI)@FTO** displayed new peaks at 182.3 eV and 184.7 eV corresponding to Zr 3d of the UiO-framework.[72–73] Additionally, both the film and monolayer showed a C1s peak around 288.0 eV, which can be associated with the carbonyl groups of the NDI core (Figure S9).[74–75] The C1s and N1s peaks attributed to NDI are slightly shifted towards higher binding energy in the case of **Zr(dcphOH-NDI)@FTO**, presumably due to coordination of the NDI linker to the Zr-oxo components with the SBUs within the framework.

Electrochemical and Optical Properties

A summary of the electrochemical and optical properties of the NDI-MOF thin films is shown in Table 1. Cyclic voltammograms (CVs) of **Zr(dcphOH-NDI)@FTO** thin films and **dcphOH-NDI** in solution for comparison were recorded in DMF using 0.8 M KPF_6 as the supporting electrolyte (Figure 6a) and clearly show two reversible couples in the cathodic scan at $E_{1/2}$ = −0.96 V and −1.36 V vs. $Fc^{+/0}$, consistent with sequential one-electron reductions on the NDI core (NDI/NDI$^{·−}$ and NDI$^{·−/2−}$) These values match well with the half-wave potentials recorded for the linker in solution (Figure S10). Additionally, because the Zr(IV) centers have a d^0 electron configuration and are redox inactive, the Faradic response in the CVs is exclusively attributed to the NDI linkers. During the first successive scans, the current density slowly increases until reaching a maximum after 20 cycles (Figure 6b). This conditioning effect has been shown in other MOF-modified electrodes and can be explained as the ingress of supporting electrolyte into the framework as the result of an applied potential, which increases the local concertation of available counter ions.[46] The integrity of the framework was maintained during electrochemical conditioning, as shown by PXRD patterns of the films before and after cycling (Figure S11). Coulometry measurements (Figure S12) estimated the amount of electroactive NDI molecules in the film and resulted in an electroactive surface coverage of $3.1x10^{−7}$ mol cm$^{−2}$. By comparison, integration of the current from a CV of only the SAM on FTO resulted in a surface concentration of $7.9x10^{−11}$ mol cm$^{−2}$ (Figure S13).

It is well known that MOFs in electrochemical applications often operate by an electron hopping mechanism between fixed sites, i.e. redox-active linkers,[76–80] where charge transport can be viewed as the diffusion of electrons through the material.[81–82] In addition, the transport of ions or supporting electrolyte is required to balance charge upon oxidation or reduction of the framework. Combined with the hopping mechanism of localized charge carries, this creates a situation of diffusion-like charge transport through the porous material, depending on an equivalent diffusion coefficient, D_e.[83–85] In the case of electrocatalytic MOFs,[17] if the catalytic reaction and substrate diffusion within the framework are

comparatively fast, the catalytic current will be limited by D_e.[83–84] Thus, it is vitally important for MOFs in electrocatalytic applications to have fast electron transport as well as facile movement of counter ions throughout the material. Notably, the CVs of Zr(dcphOH-NDI)@FTO films take the form of diffusion waves. Upon varying the scan rate (Figure 7), this was confirmed by plots of peak current density (j_{pc}) vs. the square root of the scan rate ($\nu^{1/2}$) in Figures 7c and d, where a linear relationship was obtained at the first and second reduction. When linear diffusion is the sole mode of transport, i_{pc} is proportional to $\nu^{1/2}$, and the voltammetric response is described by eq. (1),

$$i_{pc} = 0.446 F A C° \sqrt{D_e} \sqrt{\frac{Fv}{RT}} \quad (1)$$

where F is Faraday's constant, ν is the scan rate, A is the surface area of the electrode, $C°$ is the concentration of redox active species within the film, R is the universal gas constant, T is the temperature, and D_e is the equivalent diffusion coefficient. It follows that the process of electron transfer through the film is diffusion limited via the combined effect of electron hopping between NDI linkers and mass transport of counter ions through the pores of the framework, giving rise to D_e (*vide infra*). The large non-zero peak separation $E_p = 166$ mV and 175 mV for the first and second reduction respectively also reflects slow electron transfer through the framework A rapid surface-confined process will display a $E_p = 0$, and in the ideal case of a fully reversible (one-electron) diffusion-controlled process, $E_p = 57$ mV at 25 °C.

UV-vis spectroelectrochemistry was used to observe the spectral changes of **Zr(dcphOH-NDI)@FTO** upon reduction and probe the kinetics of electron transfer within the film. Steady-state UV-vis spectra of **Zr(dcphOH-NDI)@FTO** thin films display characteristic π-π* absorption bands of the NDI core at 364 and 382 nm (Figure S14). At applied potentials, we see the disappearance of these bands and the appearance of new absorptions in the visible region, resulting in defined color changes in the film (Figure 8). When the potential is held at −1.26 V, new bands are seen at 475, 608, and 780 nm, assigned to the formation of the NDI$^{·-}$ species. At −1.76 V, the absorption at 475 nm decreases, while a new pair of bands appears at 394 and 416 nm, concomitant with an increase in intensity at 608 nm. These new transitions suggest the formation of NDI^{2-}, and all assignments were corroborated by UV-vis spectra obtained from the free NDI linker at similar potentials (Figure S15). Additionally, by comparing the initial concentration of NDI inside the framework to the final concentration of reduced NDI$^{·-}$, we determined that approximately 97% of the NDI linkers in the film are redox-active at an applied potential of −1.26 V (see Supporting Information). In previously reported UiO-based electrodes, the fraction of electroactive linkers ranges from 1% to 32%.[34–35] The electrochromism of the films upon reduction is reversible and the color returns when oxidized back to the NDI0 species. To demonstrate this, the potential was stepped between 0 V and −1.3 V for 5 cycles while the absorbance change (Abs) at 475 nm was monitored (Figure S16). This demonstrates that the reversible electrochromic behavior is retained after multiple cycles.

The kinetics of electron transport through the films could be followed by spectroelectrochemical measurements. By monitoring the absorbance at 475 nm corresponding to the reduced form of the NDI linker, the concentration of reduced species inside the framework can be directly measured as a function of time. Plotting Abs vs. $t^{1/2}$ then results in a linear relationship and allows for measuring the equivalent diffusion coefficient via the form of the Cottrell equation[76, 86] given in eq. 2 where,

$$\Delta\, Abs = \frac{2 A_{max}\sqrt{D_e t}}{d_f \sqrt{\pi}} \quad (2)$$

A_{max} is the absorbance maximum, t is time in second, and d_f is the thickness of the film. For **Zr(dcphOH-NDI)@FTO** thin films, this resulted in an equivalent diffusion coefficient $D_e(KPF_6) = 5.4\pm1.1 \times 10^{-11}$ cm^2 s^{-1} (Figure S17). This is considerably higher than other MOF-based electrodes with redox-active linkers measured in non-aqueous solvents (10^{-12} - 10^{-13} cm^2 s^{-1}),[8–9, 76, 87] and indicates that electron hopping and mass transport through the films is relatively fast. The effect of mass transport within the film was further investigated by varying the size of counter cation in the supporting electrolyte, which must be transported through the pores during reduction of the framework to allow charge equilibration. Examining the same set of films under identical conditions while only changing the supporting electrolyte from KPF$_6$ ($r_{K^+} = 1.33$ Å)[88] to n-Bu$_4$NPF$_6$ ($r_{n-Bu_4N^+} = 4.94$ Å),[89] the equivalent diffusion coefficient decreased significantly by about one order of magnitude ($D_e(n$-Bu$_4$NPF$_6) = 4.0\pm2.5 \times 10^{-12}$ cm^2 s^{-1}), concordant with the increase in size of the cation (Figure S16c). Interestingly, when using KPF$_6$, plots of the Abs at 475 nm vs. t under -1.31 V applied potential (Figure S16b) show the absorbance reaching a plateau after 400s, corresponding to a maximum concentration of NDI$^{\cdot-}$ in the film. Conversely, the same films measured in solutions with n-Bu$_4$NPF$_6$ show a continual increase in absorbance at 475 nm over 400 s, suggesting an incomplete reduction of the NDI linkers on the time scale of the experiment. This indicates that the large size of n-Bu$_4$N$^+$ impedes transport within the pores of the framework, reflected by the decreases in D_e, and consequently the film is only partially reduced. Thus, we have shown that charge and mass transport through redox-active MOF films are potential current-limiting phenomena that must be carefully controlled by experimental parameters (counter ion size, porosity, redox activity, film thickness, etc.) for such films to function optimally in electrocatalytic applications.

As the electrocatalytic applications that we envisage for our platform in the future (for example proton reduction) may operate in aqueous solutions, we also tested the electrochemical behavior of **Zr(dcphOH-NDI)@FTO** films using an aqueous 0.8 M KCl (pH = 6.5) solution as supporting electrolyte. Interestingly, the two sequential waves that are observed in the CV of **Zr(dcphOH-NDI)@FTO** films in DMF collapse to a single reversible reduction wave at -0.24 V vs. NHE (-0.90 V vs. Fc$^{+/0}$ (Figure S18a)) in 0.8 M KCl$_{(aq)}$. Previous reports of homogeneous NDI derivatives have shown a solvent-dependent anodic shift of the NDI$^{\cdot-}$/NDI^{2-} couple in the presence of K$^+$, Li$^+$ or Mg^{2+} cations that result from a stabilizing interaction between the NDI^{2-} species and the cation at the imide oxygen atoms.[90–92] At high cation concentrations, the two one-electron reduction waves

were observed to merge into a single two-electron process.91 This situation reflects that in the pores of **Zr(dcphOH-NDI)@FTO**, and we propose a similar interaction between the K$^+$ ions and the NDI linkers in an aqueous environment to give rise to the observed single reduction wave in the CVs.

Upon cycling the film between 0.7 V and –0.8 V vs. NHE at 100 mVs^{-1} (Figure S18b), the current density decreases over the first few scans, presumably due to partial film delamination. After 20 cycles, the current density stabilizes and overlapping successive scans are recorded. From scan rate dependent CVs (Figure S19), the peak current density varies linearly with $\nu^{1/2}$, indicating a diffusion-controlled charge transfer process also in aqueous solution. Remarkably, spectroelectrochemical measurements (Figure S20) reveal an order of magnitude increase in the diffusion coefficient, D_e(KCl$_{(aq)}$) = 2.1x10^{-10} cm^2 s^{-1}, with a comparable electroactive surface concentration (1.2x10^{-7} mol cm^{-2}) as compared to that measured in DMF with K$^+$ as the cation. Digesting the MOF thin films after measuring the electroactive surface concentration by coulometry yielded the percentage of redox-active linkers as 87% (see Supporting Information). In addition, the number of transferred electrons was calculated as $n = 1.7$, indicating that the single reduction wave observed in the CVs is indeed a two-electron process.

Conclusion

Designing redox-active MOFs that can be synthesized as thin films is a key challenge towards their application in electrocatalysis. Here, we have developed a novel MOF-based thin film platform that provides electron transport pathways close to the operating potential of many proton reduction catalysts. Importantly, this system is derived from a robust, Zr-based MOF that exhibits a high surface area and large pore size, necessary for efficient transport of substrates, products, and counter ions. The pK_a of both the proton-responsive NDI linker and the Zr-node demonstrate potential use in PCET over a wide pH range (3.4 – 6.1). When grown on conducting substrates, this material forms thin films that display reversible electrochromic behavior. Electrochemical experiments showed this corresponds to the sequential one-electron reductions of the redox-active NDI linkers within the framework. Importantly, nearly all (97%) of the NDI sites are electrochemically active at applied potential. The method of charge transport within the films was determined to be diffusion limited, in agreement with the electron hopping model common to many MOF-based thin films. Finally the MOF thin films were found to function efficiently in aqueous solutions, adding to their potential usefulness in electrocatalytic applications.

This work represents a significant advancement in the development of redox active MOFs and MOF thin films. To date, reports of catalytic MOFs featuring redox active linkers are almost exclusively based on porphyrins with limited routes for linker exchange or functionalization.8–9, 76 Attainment of the UiO/PIZOF-type structure with **Zr(dcphOH-NDI)@FTO** confers unprecedented versatility to utilize postsynthetic methods to introduce catalytic units into a robust and widely studied framework that can now be rendered redox active. This is enabled by decoupling the redox hopping mechanism through the film from the sites of catalysis. Ongoing work is underway to incorporate molecular catalysts into **Zr(dcphOH-NDI)@FTO** thin films for the electrocatalytic conversion of small molecules.

Experimental Section

Materials and Methods

All solvents and commercially supplied chemicals were reagent grade and used as received without further purification. $ZrCl_4$ (99.99%), tetrabutylammonium hexafluorophosphate (*n*-Bu_4NPF_6, for electrochemical analysis, 99.0%), potassium hexafluorophosphate (KPF_6, 99.0%), 4-amino-3-hydroxybenzoic acid (97%), and fluorine-doped tin oxide (FTO) substrates (7 Ω/sq) were purchased from Sigma-Aldrich. Naphthalene-1,4,5,8-tetracarboxylic dianhydride (98.0%) was purchased from TCI. Glacial acetic acid, and N,N-dimethylformamide (DMF) (99.9%) were purchased from VWR. ^{1}H-NMR spectra were measured using a JEOL 400 MHz spectrometer at 293 K. The chemical shifts given in ppm are internally referenced to the residual solvent signal. MOF samples were digested prior to NMR measurement by addition of 25 μL of HF to a suspension of 10 mg of MOF in 0.575 mL of DMSO-d_6. ESI-MS data were collected on a Thermo LCQ XP Max mass spectrometer in negative mode with electrospray ionization. Electronic absorption spectra were measured using a Varian Cary 50 UV-Vis spectrophotometer. ATR-FTIR data were collected on a Bruker ALPHA FTIR Spectrometer from 4000 cm^{-1} to 450 cm^{-1} at room temperature.

dcphOH-NDI

3-Hydroxy-2-[7-(4-carboxy-2-hydroxyphenyl)-1,3,6,8-tetraoxo-3,6,7,8-tetrahydro-1H-benzo [lmn] [3,8] phenanthrolin-2-yl]-benzoic acid (dcphOH-NDI) was synthesized following a reported procedure.[93] A round bottom flask attached to a reflux condenser was charged with 4-amino-3-hydroxybenzoic acid (1.01 g, 6.6 mmol) and naphthalene-1,4,5,8-tetracarboxylic dianhydride (0.804 g, 3 mmol). DMF (20 mL) was added and the reaction was placed under Ar atmosphere. The resulting dark-red solution was refluxed overnight. After the reaction mixture was cooled to room temperature, 5 mL of 1 M HCl was added, and the product was precipitated by adding the solution dropwise into ice-cooled water (250 mL). The pale-yellow precipitate was collected by centrifugation and washed with ethanol, water, and ether (25 mL each) and dried under vacuum. Yield: 1.15 g (71%). ^{1}H NMR (400 MHz, DMSO-d_6) δ ppm: 7.43 - 7.49 (m, 2 H) 7.50 - 7.56 (m, 2 H) 7.56 - 7.60 (m, 2 H) 8.59 - 8.88 (m, 4 H) 10.17 (s, 2 H). ESI-MS(−) (MeOH/THF 1:1 v/v): [M-H]$^-$, *m/z* = 536.99 (calc. *m/z* = 537.06); [M-COOH]$^-$, *m/z* = 493.25 (calc. *m/z* = 493.07).

Zr(dcphOH-NDI) MOF bulk synthesis

In a 20 mL scintillation vial $ZrCl_4$ (82 mg, 0.35 mmol), dcphOH-NDI (177.3 mg, 0.35 mmol), and 0.602 mL (10.5 mmol) of glacial acetic acid were combined in 4 mL DMF. The contents of the vial were sonicated for 10 min. before placing in a pre-heated 120 °C oven for 72 h. The reaction was allowed to cool to room temperature, and the pale-yellow precipitate was collected by centrifugation and washed three times with DMF, followed by incubation in DMF for 24 h. The solvent was then exchanged for MeOH by washing three times and incubation in MeOH until further use. The bulk microcrystalline powders were activated by degassing under vacuum at 85 °C for 12 h.

Zr(dcphOH-NDI)@FTO MOF thin film synthesis

FTO slides were cut into 2x1 cm^2 slides and cleaned by sonication successively in solutions of Alconox, ethanol, and acetone. Cleaned FTO slides were immersed in a solution of 1 mM dcphOH-NDI in DMF overnight to form a self-assembled mono-layer (SAM). A solution of $ZrCl_4$ (23.3 mg, 0.10 mmol), dcphOH-NDI (53.8 mg, 0.10 mmol) and 171 μL of glacial acetic acid (3 mmol) in 8 mL of DMF was prepared in a 20 mL scintillation vial and sonicated for 10 min. A single slide of SAM-modified FTO was inserted and the vial was placed into a pre-heated 120 °C oven for 72 h. The vials were allowed to cool to room temperature, and the films were washed with DMF and ethanol and allowed to soak in DMF until further use.

Powder X-ray Diffraction

Powder X-ray diffraction patterns (PXRD) were obtained using a Simons D5000 Diffractometer (Cu Kα, λ = 0.15418 nm) at 45 kV and 40 mA, using a step size of 0.02°. The diffractometer was equipped with parallel beam optics (mirror + mirror) for grazing-incidence XRD measurements.

Scanning Electron Microscopy

Scanning electron microscopy (SEM) images were obtained using a Zeiss 1550 Schottky field-emission scanning electron microscope equipped with an InLens detector at 5kV acceleration voltage. MOF thin film and powder samples were anchored to conductive carbon tape on a sample holder disk and coated using a Pd-Ir-sputter coater for 30 s.

Electrochemistry

Cyclic voltammetry (CV) and chronocoulometry were performed using a one-compartment, three-electrode configuration connected to an Autolab PGSTAT100 potentiostat controlled with GPES 4.9 software (EcoChemie). For thin film measurements, the electrode setup included an auxiliary glassy carbon disc (0.071 cm^2) working electrode, which was used to monitor the solution between scans of Zr(dcphOH-NDI)@FTO thin films, a glassy carbon rod counter electrode, and a non-aqueous Ag/Ag(NO_3) (0.01 M in acetonitrile) reference electrode, referenced to the ferrocenium/ferrocene couple ($Fc^{+/0}$). Zr(dcphOH-NDI)@FTO thin films were measured in 5 mL DMF solutions as the working electrode using 0.8 M KPF_6 or n-Bu_4NPF_6 as the supporting electrolyte. Solution-phase measurements of the linker were performed at a concentration of 1 mM in DMF using a GC disk working (0.071 cm^2) electrode with 0.1 M n-Bu_4NPF_6 as the supporting electrolyte. UV-Vis spectroelectrochemistry experiments were performed on the thin film samples in a 10 mm pathlength quartz cuvette using a Pt wire counter electrode, and a non-aqueous Ag/Ag(NO_3) (0.01 M in acetonitrile) reference electrode in DMF with either 0.8 M KPF_6 or n-Bu_4NPF_6. Solution-phase spectroelectrochemistry experiments were carried out in a 1 mm pathlength cuvette using a 1 cm^2 Pt mesh working electrode, Pt wire counter electrode, and a non-aqueous Ag/Ag(NO_3) (0.01 M in acetonitrile) reference electrode in DMF with 0.1 M n-Bu_4NPF_6. For experiments in aqueous solution, 0.8 M KCl was used as the supporting electrolyte. Potential were reference to a Ag/AgCl (3 M KCl) reference electrode (+0.210 V vs. NHE). Conversion to vs. $Fc^{+/0}$ was performed using a reported value.[94]

Gas adsorption

N_2 adsorption isotherms were measured at 77 K (liquid N_2 bath) using a Micromeritics ASAP 2060 micropore physisorption analyzer. The bulk powder samples were activated under dynamic vacuum (1×10^{-4} Pa) at 85 °C, using a Micromeritic SmartVacPrep sample preparation unit. The cold and warm free space of the sample tubes was determined using He gas.

Potentiometric Titrations

Acid-base titrations of **dcphOH-NDI** and **Zr(dcphOH-NDI)** were performed according to a reported procedure.70 ~50 mg of MOF sample (ground with a mortar and pestle) was suspended in 60 mL of 0.01 M $NaNO_3$ (aq.) overnight. The solution was placed in a glass electrochemical cell (100 mL) equipped with a SevenCompact S220 pH/ion meter (Mettler Toledo) and a stir bar. Prior to titration, the meter was calibrated with commercial (Mettler Toldeo) buffer solutions at pH = 4.01, 7.00, and 9.21. The pH of the suspension was adjusted with 0.1 M HCl to an initial pH of 3. Then aliquots of 25 μL of 0.1 M NaOH were added while stirring and the pH was recorded once the voltage stabilized to a final pH of 8.6. The addition rate was approximately 0.024 mL min^{-1}. In the case of the free linker (**dcphOH-NDI**), 17 mg of compound in a 25 mL solution of 0.01 M $NaNO_3$ (aq)/DMF (1:1; v/v) was used, and titrated to a final pH of 11. Equivalence points were calculated from local maxima in the first derivative of the titration curve, and the corresponding pK_a values are then equal to the pH at 0.5 times the volume of NaOH added to reach the equivalence point.

X-ray Photoelectron Spectroscopy

X-ray photoelectron spectroscopy (XPS) spectra were recorded on a PHI Quantera II sacanning XPS microprobe with monochromated Al Kα radiation (1486.6 eV). Shifts in binding energy were corrected using the C1s peak as an internal standard at 284.6 eV. Survey spectra were recorded at a pass energy of 244 eV with a step size of 0.2 eV, while for high-resolution spectra a pass energy of 55 eV and step size of 0.05 eV were used.

Thermogravimetric Analysis

Thermogravimetric analysis (TGA) was performed on a TA instruments Q500 thermogravimetric analyzer under a flow of air (50 mL min^{-1}) from 25 °C to 800 °C at a rate of 5 °C min^{-1} Prior to measurement MOF samples were dried at 120 °C for 20 h under N_2.

Supplementary Material

Refer to Web version on PubMed Central for supplementary material.

Acknowledgement

References

(1). Furukawa H, Cordova KE, O'Keeffe M, Yaghi OM. Science. 2013; 341

(2). Kuppler RJ, Timmons DJ, Fang Q-R, Li J-R, Makal TA, Young MD, Yuan D, Zhao D, Zhuang W, Zhou H-C. Coord Chem Rev. 2009; 253:3042–3066.

(3). Yaghi OM, O'Keeffe M, Ockwig NW, Chae HK, Eddaoudi M, Kim J. Nature. 2003; 423:705–714. [PubMed: 12802325]

(4). Deria P, Mondloch JE, Karagiaridi O, Bury W, Hupp JT, Farha OK. Chem Soc Rev. 2014; 43:5896–5912. [PubMed: 24723093]

(5). Wang Z, Cohen SM. Chem Soc Rev. 2009; 38:1315–1329. [PubMed: 19384440]

(6). Cohen SM. J Am Chem Soc. 2017; 139:2855–2863. [PubMed: 28118009]

(7). Wang C, Xie Z, deKrafft KE, Lin W. J Am Chem Soc. 2011; 133:13445–13454. [PubMed: 21780787]

(8). Hod I, Sampson MD, Deria P, Kubiak CP, Farha OK, Hupp JT. ACS Catal. 2015; 5:6302–6309.

(9). Kornienko N, Zhao Y, Kley CS, Zhu C, Kim D, Lin S, Chang CJ, Yaghi OM, Yang P. J Am Chem Soc. 2015; 137:14129–14135. [PubMed: 26509213]

(10). Usov PM, Huffman B, Epley CC, Kessinger MC, Zhu J, Maza WA, Morris AJ. ACS Appl Mater Interfaces. 2017; 9:33539–33543. [PubMed: 28353341]

(11). Usov PM, Ahrenholtz SR, Maza WA, Stratakes B, Epley CC, Kessinger MC, Zhu J, Morris AJ. J Mater Chem A. 2016; 4:16818–16823.

(12). Chambers MB, Wang X, Elgrishi N, Hendon CH, Walsh A, Bonnefoy J, Canivet J, Quadrelli EA, Farrusseng D, Mellot-Draznieks C, Fontecave M. ChemSusChem. 2015; 8:603–608. [PubMed: 25613479]

(13). Kajiwara T, Fujii M, Tsujimoto M, Kobayashi K, Higuchi M, Tanaka K, Kitagawa S. Angew Chem Int Ed. 2016; 55:2697–2700.

(14). Fei H, Sampson MD, Lee Y, Kubiak CP, Cohen SM. Inorg Chem. 2015; 54:6821–6828. [PubMed: 26135673]

(15). Kung C-W, Mondloch JE, Wang TC, Bury W, Hoffeditz W, Klahr BM, Klet RC, Pellin MJ, Farha OK, Hupp JT. ACS Appl Mater Interfaces. 2015; 7:28223–28230. [PubMed: 26636174]

(16). Ji P, Solomon JB, Lin Z, Johnson A, Jordan RF, Lin W. J Am Chem Soc. 2017; 139:11325–11328. [PubMed: 28797163]

(17). Downes CA, Marinescu SC. ChemSusChem. 2017; 10:4374–4392. [PubMed: 28968485]

(18). Solomon MB, Church TL, D'Alessandro DM. CrystEngComm. 2017; 19:4049–4065.

(19). Stassen I, Burtch N, Talin A, Falcaro P, Allendorf M, Ameloot R. Chem Soc Rev. 2017; 46:3185–3241. [PubMed: 28452388]

(20). Roy S, Pascanu V, Pullen S, Gonzalez Miera G, Martin-Matute B, Ott S. Chem Commun. 2017; 53:3257–3260.

(21). Sun L, Campbell MG, Dinc M. Angew Chem Int Ed. 2016; 55:3566–3579.

(22). D'Alessandro DM. Chem Commun. 2016; 52:8957–8971.

(23). Narayan TC, Miyakai T, Seki S, Dinc M. J Am Chem Soc. 2012; 134:12932–12935. [PubMed: 22827709]

(24). Park SS, Hontz ER, Sun L, Hendon CH, Walsh A, Van Voorhis T, Dinc M. J Am Chem Soc. 2015; 137:1774–1777. [PubMed: 25597934]

(25). Sun L, Hendon CH, Minier MA, Walsh A, Dinc M. J Am Chem Soc. 2015; 137:6164–6167. [PubMed: 25932955]

(26). Talin AA, Centrone A, Ford AC, Foster ME, Stavila V, Haney P, Kinney RA, Szalai V, El Gabaly F, Yoon HP, Léonard F, et al. Science. 2014; 343:66–69. [PubMed: 24310609]

(27). Han S, Warren SC, Yoon SM, Malliakas CD, Hou X, Wei Y, Kanatzidis MG, Grzybowski BA. J Am Chem Soc. 2015; 137:8169–8175. [PubMed: 26020132]

(28). Clough AJ, Yoo JW, Mecklenburg MH, Marinescu SC. J Am Chem Soc. 2015; 137:118–121. [PubMed: 25525864]

(29). Zhao S, Wang Y, Dong J, He C-T, Yin H, An P, Zhao K, Zhang X, Gao C, Zhang L, Lv J, et al. Nat Energy. 2016; 1:16184.

(30). Cavka JH, Jakobsen S, Olsbye U, Guillou N, Lamberti C, Bordiga S, Lillerud KP. J Am Chem Soc. 2008; 130:13850–13851. [PubMed: 18817383]

(31). Schaate A, Roy P, Godt A, Lippke J, Waltz F, Wiebcke M, Behrens P. Chem Eur J. 2011; 17:6643–6651. [PubMed: 21547962]

(32). DeCoste JB, Peterson GW, Jasuja H, Glover TG, Huang Y-g, Walton KS. J Mater Chem A. 2013; 1:5642–5650.

(33). Mondloch JE, Katz MJ, Planas N, Semrouni D, Gagliardi L, Hupp JT, Farha OK. Chem Commun. 2014; 50:8944–8946.

(34). Johnson BA, Bhunia A, Ott S. Dalton Trans. 2017; 46:1382–1388. [PubMed: 27845800]

(35). Lin S, Pineda-Galvan Y, Maza WA, Epley CC, Zhu J, Kessinger MC, Pushkar Y, Morris AJ. ChemSusChem. 2017; 10:514–522. [PubMed: 27976525]

(36). Kim M, Cahill JF, Su Y, Prather KA, Cohen SM. Chem Sci. 2012; 3:126–130.

(37). Pullen S, Fei H, Orthaber A, Cohen SM, Ott S. J Am Chem Soc. 2013; 135:16997–17003. [PubMed: 24116734]

(38). Mijangos E, Roy S, Pullen S, Lomoth R, Ott S. Dalton Trans. 2017; 46:4907–4911. [PubMed: 28345708]

(39). Fei H, Pullen S, Wagner A, Ott S, Cohen SM. Chem Commun. 2015; 51:66–69.

(40). Kobaisi MA, Bhosale SV, Latham K, Raynor AM, Bhosale SV. Chem Rev. 2016; 116:11685–11796. [PubMed: 27564253]

(41). Facchetti A. Mater Today. 2013; 16:123–132.

(42). Zhan X, Facchetti A, Barlow S, Marks TJ, Ratner MA, Wasielewski MR, Marder SR. Adv Mater. 2011; 23:268–284. [PubMed: 21154741]

(43). Costentin C, Drouet S, Passard G, Robert M, Savéant J-M. J Am Chem Soc. 2013; 135:9023–9031. [PubMed: 23692448]

(44). Weinberg DR, Gagliardi CJ, Hull JF, Murphy CF, Kent CA, Westlake BC, Paul A, Ess DH, McCafferty DG, Meyer TJ. Chem Rev. 2012; 112:4016–4093. [PubMed: 22702235]

(45). Mulfort KL, Hupp JT. J Am Chem Soc. 2007; 129:9604–9605. [PubMed: 17636927]

(46). Wade CR, Li M, Dinc M. Angew Chem. 2013; 125:13619–13623.

(47). Leong CF, Chan B, Faust TB, D'Alessandro DM. Chem Sci. 2014; 5:4724–4728.

(48). Ma B-Q, Mulfort KL, Hupp JT. Inorg Chem. 2005; 44:4912–4914. [PubMed: 15998017]

(49). Wade CR, Corrales-Sanchez T, Narayan TC, Dinca M. Energy Environ Sci. 2013; 6:2172–2177.

(50). Usov PM, Fabian C, D'Alessandro DM. Chem Commun. 2012; 48:3945–3947.

(51). Garai B, Mallick A, Banerjee R. Chem Sci. 2016; 7:2195–2200.

(52). Haldar R, Mazel A, Joseph R, Adams M, Howard IA, Richards BS, Tsotsalas M, Redel E, Diring S, Odobel F, Wöll C. Chem Eur J. 2017; 23:14316–14322. [PubMed: 28815774]

(53). AlKaabi K, Wade, Casey R, Dinc M. Chem. 1:264–272.

(54). Marshall RJ, Kalinovskyy Y, Griffin SL, Wilson C, Blight BA, Forgan RS. J Am Chem Soc. 2017; 139:6253–6260. [PubMed: 28385019]

(55). Schaate A, Roy P, Preuße T, Lohmeier SJ, Godt A, Behrens P. Chem Eur J. 2011; 17:9320–9325. [PubMed: 21796692]

(56). Lippke J, Brosent B, von Zons T, Virmani E, Lilienthal S, Preuße T, Hülsmann M, Schneider AM, Wuttke S, Behrens P, Godt A. Inorg Chem. 2017; 56:748–761. [PubMed: 28032763]

(57). Roy P, Schaate A, Behrens P, Godt A. Chem Eur J. 2012; 18:6979–6985. [PubMed: 22508557]

(58). Marshall RJ, Griffin SL, Wilson C, Forgan RS. Chem Eur J. 2016; 22:4870–4877. [PubMed: 26916707]

(59). Doan TLH, Dao TQ, Tran HN, Tran PH, Le TN. Dalton Trans. 2016; 45:7875–7880. [PubMed: 27064371]

(60). Chen D, Xing H, Wang C, Su Z. J Mater Chem A. 2016; 4:2657–2662.

(61). Yuan S, Zou L, Qin J-S, Li J, Huang L, Feng L, Wang X, Bosch M, Alsalme A, Cagin T, Zhou H-C. Nat Commun. 2017; 8:15356. [PubMed: 28541301]

(62). Ayala S, Zhang Z, Cohen SM. Chem Commun. 2017; 53:3058–3061.

(63). Schukraft GEM, Ayala S, Dick BL, Cohen SM. Chem Commun. 2017; 53:10684–10687.

(64). Wang C, Wang J-L, Lin W. J Am Chem Soc. 2012; 134:19895–19908. [PubMed: 23136923]

(65). Bernales V, Yang D, Yu J, Gümü lü G, Cramer CJ, Gates BC, Gagliardi L. ACS Appl Mater Interfaces. 2017; 9:33511–33520. [PubMed: 28537379]

(66). Pascanu V, Yao Q, Bermejo Gómez A, Gustafsson M, Yun Y, Wan W, Samain L, Zou X, Martín-Matute B. Chem Eur J. 2013; 19:17483–17493. [PubMed: 24265270]

(67). Costentin C, Drouet S, Robert M, Savéant J-M. Science. 2012; 338:90–94. [PubMed: 23042890]

(68). Costentin C, Passard G, Robert M, Savéant J-M. J Am Chem Soc. 2014; 136:11821–11829. [PubMed: 25078392]

(69). Hod I, Deria P, Bury W, Mondloch JE, Kung C-W, So M, Sampson MD, Peters AW, Kubiak CP, Farha OK, Hupp JT. Nat Commun. 2015; 6:8304. [PubMed: 26365764]

(70). Klet RC, Liu Y, Wang TC, Hupp JT, Farha OK. J Mater Chem A. 2016; 4:1479–1485.

(71). Liu J-J, Wang Y, Hong Y-J, Lin M-J, Huang C-C, Dai W-X. Dalton Trans. 2014; 43:17908–17911. [PubMed: 25337900]

(72). Lyu J, Liu H, Zeng Z, Zhang J, Xiao Z, Bai P, Guo X. Ind Eng Chem Res. 2017; 56:2565–2572.

(73). Wang A, Zhou Y, Wang Z, Chen M, Sun L, Liu X. RSC Advances. 2016; 6:3671–3679.

(74). Moore JR, Albert-Seifried S, Rao A, Massip S, Watts B, Morgan DJ, Friend RH, McNeill CR, Sirringhaus H. Adv Energy Mater. 2011; 1:230–240.

(75). Giesbers M, Marcelis ATM, Zuilhof H. Langmuir. 2013; 29:4782–4788. [PubMed: 23548381]

(76). Ahrenholtz SR, Epley CC, Morris AJ. J Am Chem Soc. 2014; 136:2464–2472. [PubMed: 24437480]

(77). Patwardhan S, Schatz GC. J Phys Chem C. 2015; 119:24238–24247.

(78). Hod I, Bury W, Gardner DM, Deria P, Roznyatovskiy V, Wasielewski MR, Farha OK, Hupp JT. J Phys Chem Lett. 2015; 6:586–591. [PubMed: 26262471]

(79). Kung C-W, Wang TC, Mondloch JE, Fairen-Jimenez D, Gardner DM, Bury W, Klingsporn JM, Barnes JC, Van Duyne R, Stoddart JF, Wasielewski MR, et al. Chem Mater. 2013; 25:5012–5017.

(80). Kung C-W, Chang T-H, Chou L-Y, Hupp JT, Farha OK, Ho K-C. Chem Commun. 2015; 51:2414–2417.

(81). Blauch DN, Saveant JM. J Am Chem Soc. 1992; 114:3323–3332.

(82). Savéant JM. J Electroanal Chem. 1986; 201:211–213.

(83). Costentin C, Saveant J-M. J Phys Chem C. 2015; 119:12174–12182.

(84). Costentin C, Savéant J-M. ChemElectroChem. 2015; 2:1774–1784.

(85). Costentin C, Saveant J-M. PCCP. 2015; 17:19350–19359. [PubMed: 26140372]

(86). AllenJ, , BardLRF. Electrochemical Methods: Fundamentals and Applications2nd ed. John Wiley & Sons, Inc; New York: 2010

(87). Lin S, Diercks CS, Zhang Y-B, Kornienko N, Nichols EM, Zhao Y, Paris AR, Kim D, Yang P, Yaghi OM, Chang CJ. Science. 2015; 349:1208–1213. [PubMed: 26292706]

(88). PaulingL. The Nature of the Chemical Bond and the Structure of Molecules and Crystals: An Introduction to Modern Structural Chemistry2nd ed. Cornell Univ. Press; New York: 1948

(89). RobinsonRA, , StokesRH. Electrolyte Solutions2nd Rev. ed. Dover Publications; New York: 1959

(90). DeBlase CR, Hernández-Burgos K, Rotter JM, Fortman DJ, Abreu Ddos S, Timm RA, Diógenes ICN, Kubota LT, Abruña HD, Dichtel WR. Angew Chem Int Ed. 2015; 54:13225–13229.

(91). Reiner BR, Foxman BM, Wade CR. Dalton Trans. 2017; 46:9472–9480. [PubMed: 28702583]

(92). Vadehra GS, Maloney RP, Garcia-Garibay MA, Dunn B. Chem Mater. 2014; 26:7151–7157.

(93). Singh D, Baruah JB. Cryst Growth Des. 2012; 12:3169–3180.

(94). Pegis ML, Roberts JAS, Wasylenko DJ, Mader EA, Appel AM, Mayer JM. Inorg Chem. 2015; 54:11883–11888. [PubMed: 26640971]
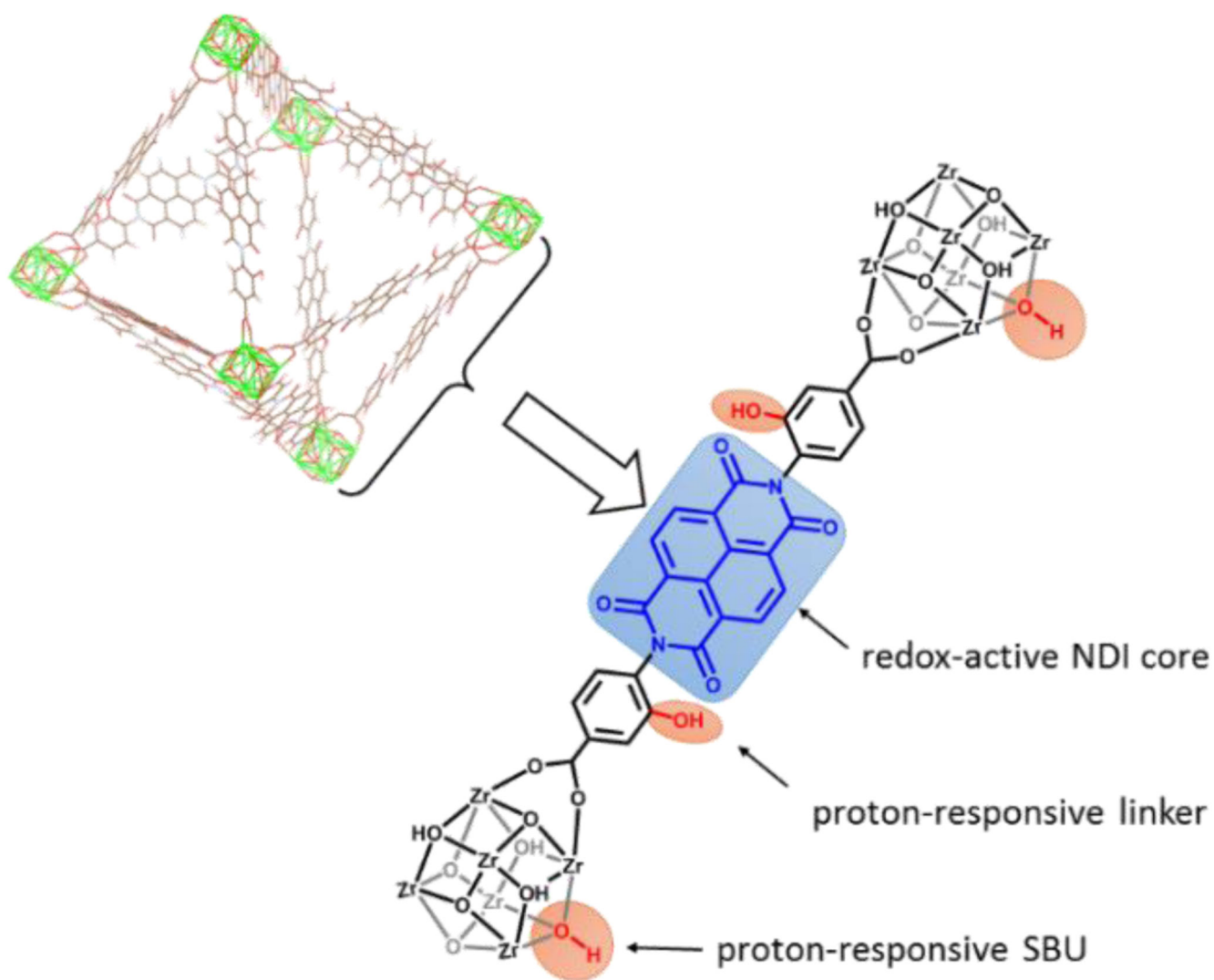
Figure 1.
MOF design strategy for developing a redox-active framework featuring UiO-topology with proton responsive functionalities.
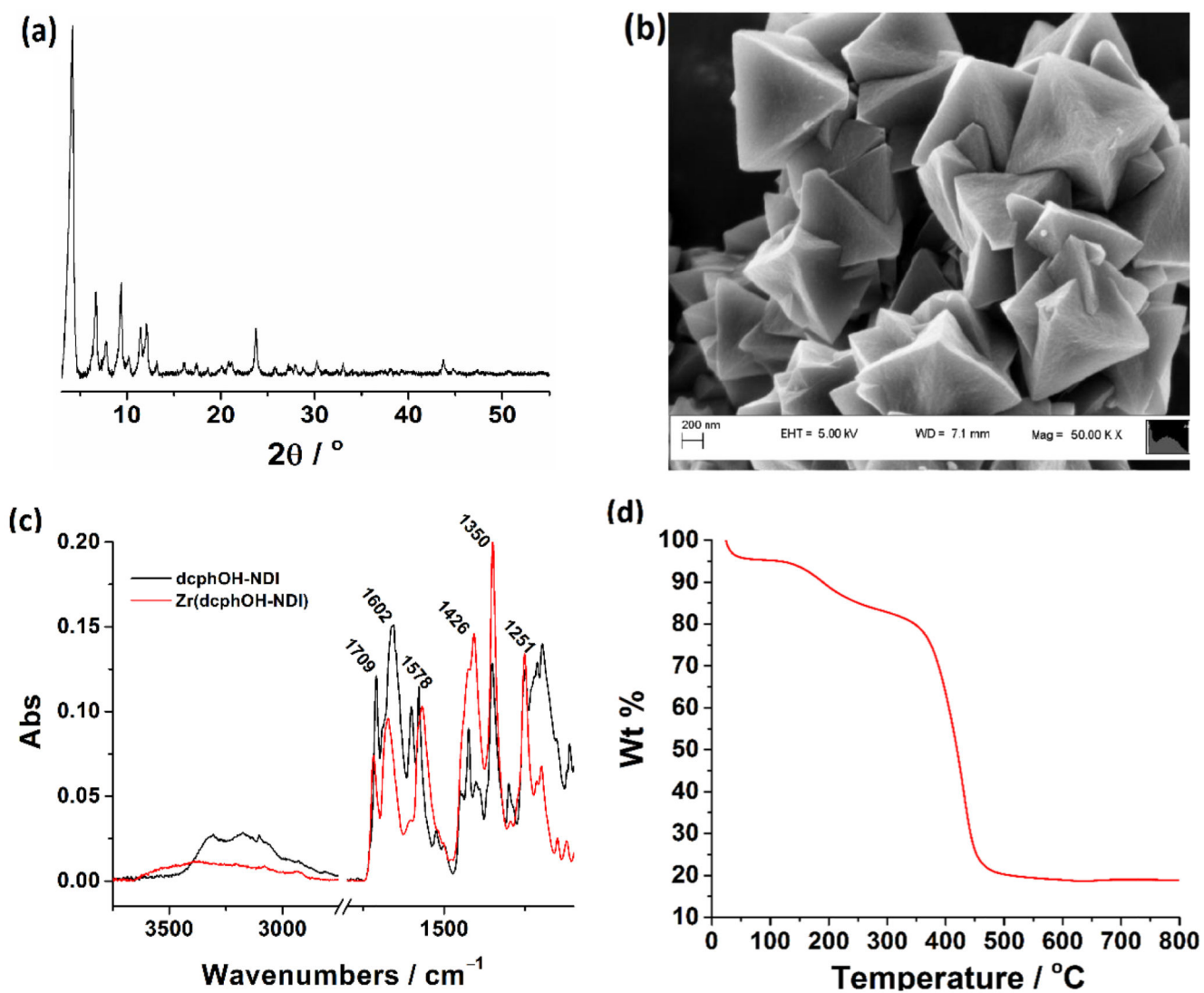
Figure 2.
Characterization of bulk microcrystalline powder **Zr(dcphOH-NDI)** by: (a) PXRD, (b) SEM imaging, (c) FTIR-ATR spectroscopy, and (d) TGA from 25-800 °C.

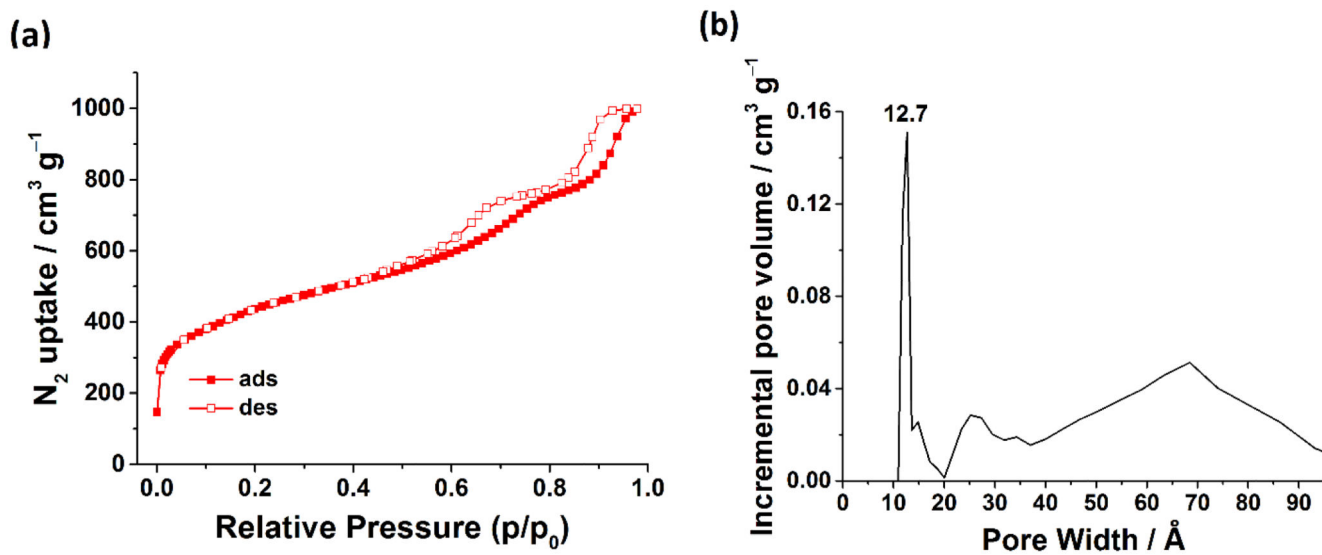**Figure 3.**
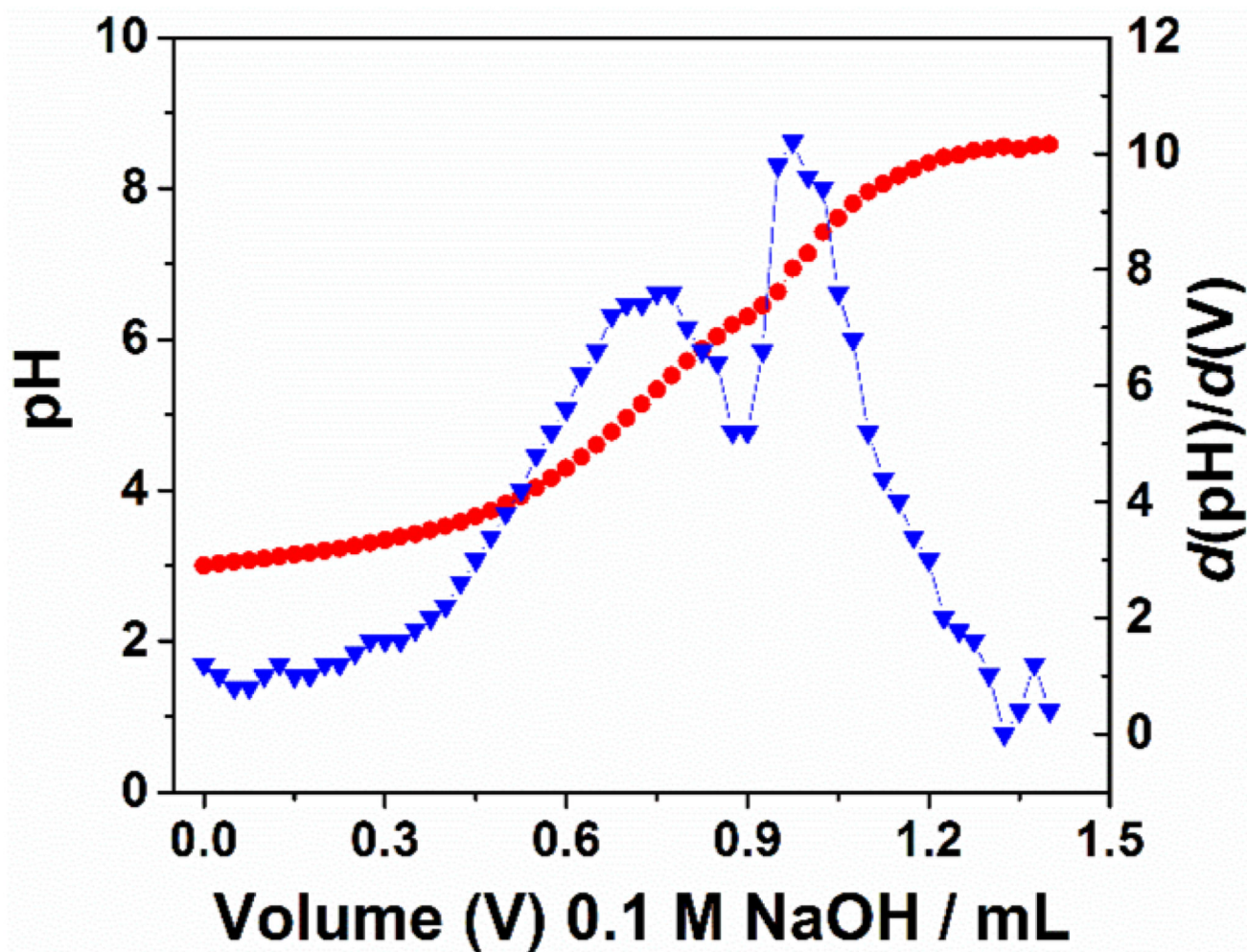(a) N_2 sorption isotherm at 77 K of **Zr(dcphOH-NDI)** and (b) corresponding pore width distribution.

Figure 4.
Acid-base titration curve for **Zr(dcphOH-NDI)** (red) and first derivative (blue).
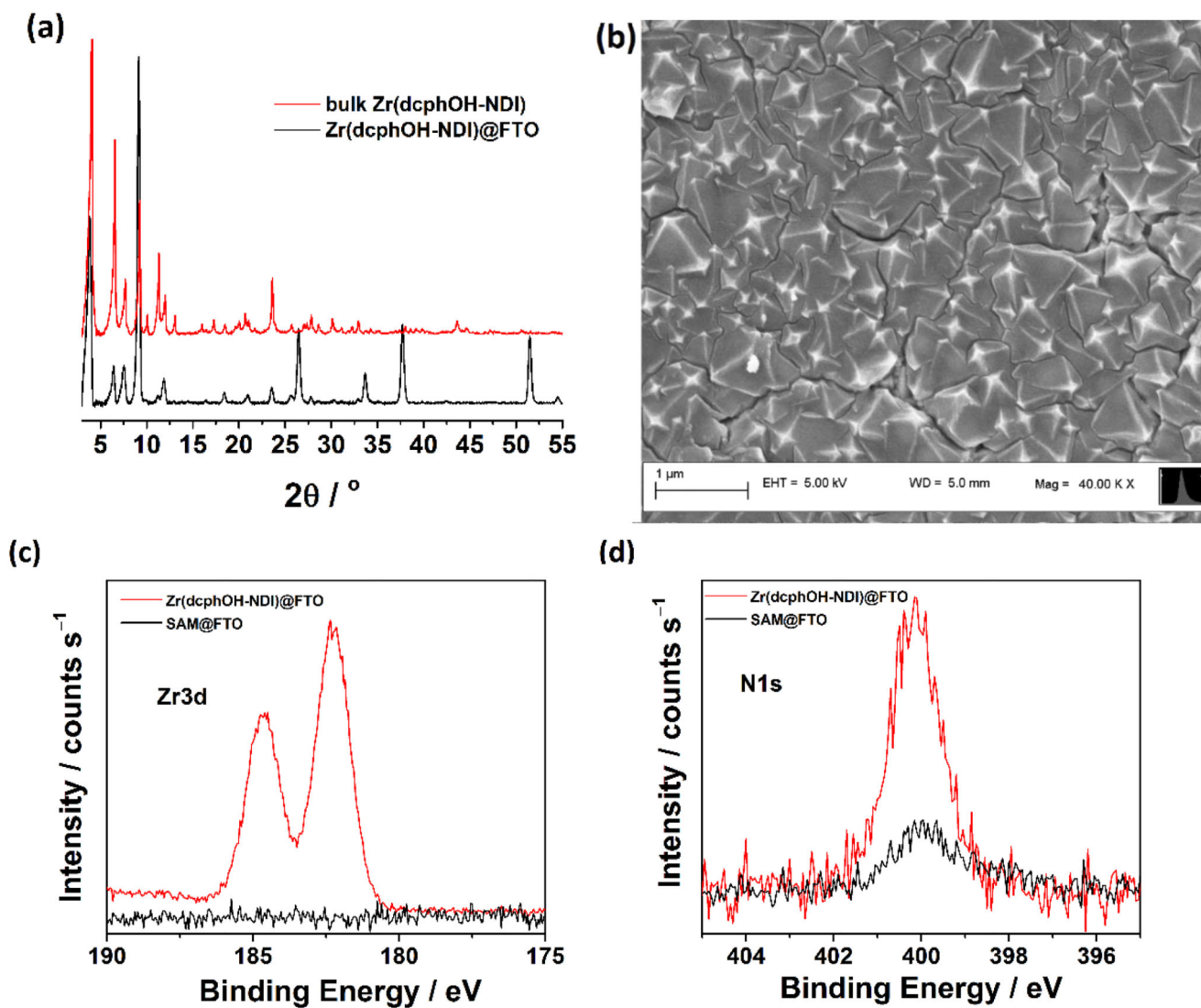
Figure 5.
(a) PXRD of **Zr(dcphOH-NDI)@FTO** films.(b) SEM image of **Zr(dcphOH-NDI)@FTO**.
XPS core-level spectra **Zr(dcphOH-NDI)@FTO** films (red) and SAM-modified FTO
(black) showing the (c) Zr₃d and (d) N1s peaks.
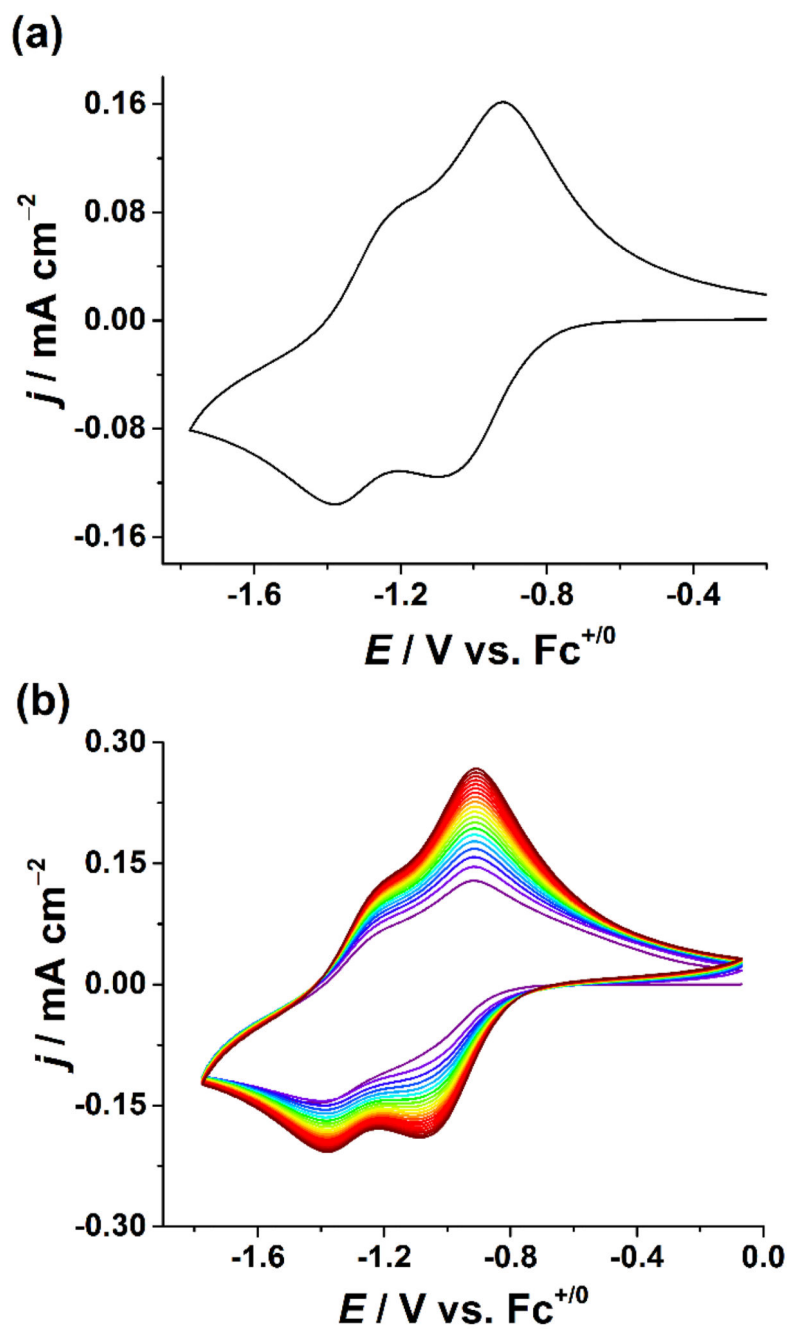
Figure 6.
CVs of **Zr(dcphOH-NDI)@FTO** thin films at (a) 50 mV s^{-1} and (b) multiple scans at 100 mV s^{-1} showing increasing current density on progressive scans.
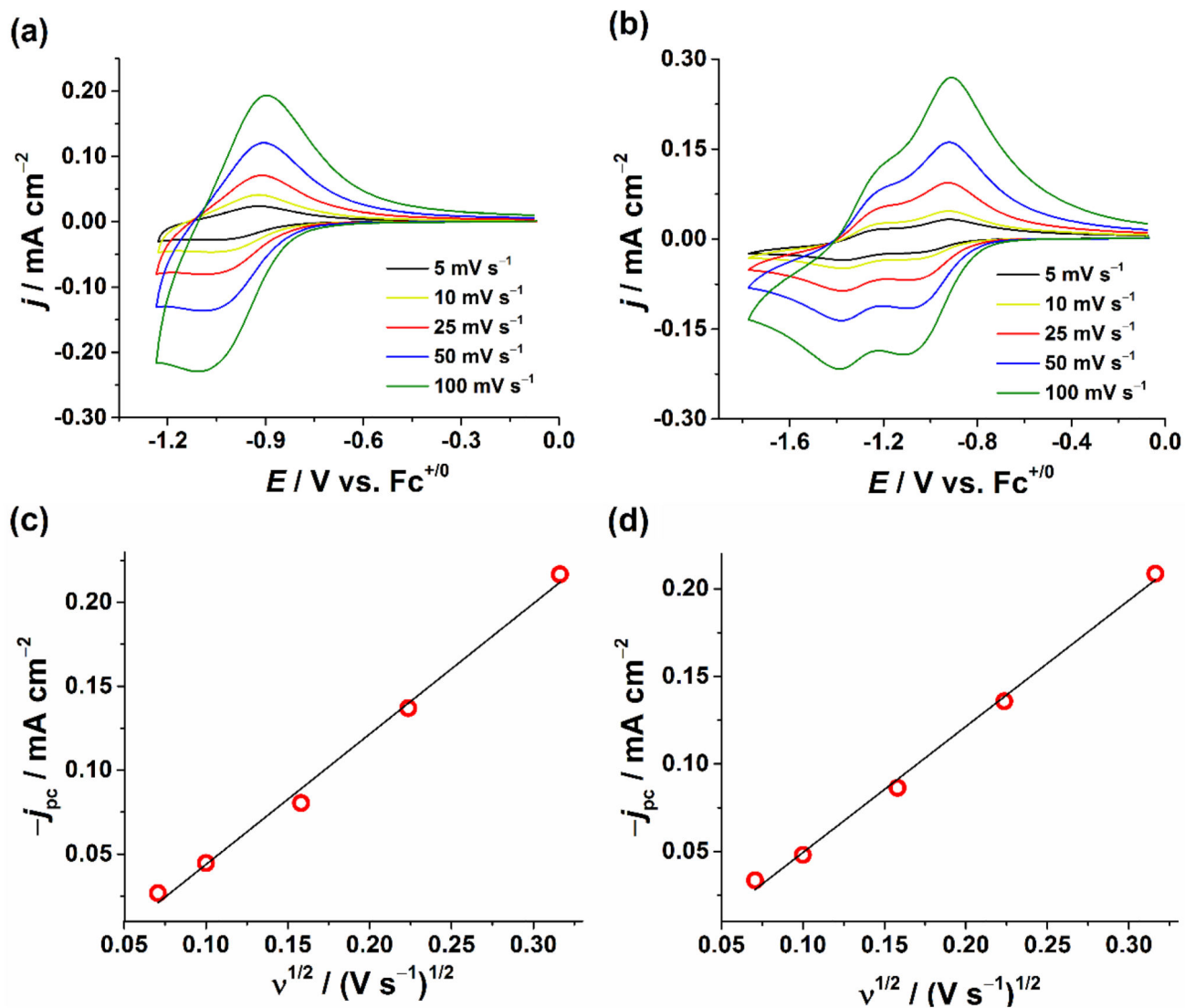
Figure 7.
Scan rate dependent CVs of **Zr(dcphOH-NDI)@FTO** upon: (a) reversing the scan after the first reduction and (b) after the second reduction at scan rates from 5 to 100 mV s^{-1}. Plots of j_{pc} vs. ν for (c) the first reduction wave and (d) the second reduction wave. The peak current density is linearly proportional to $\nu^{1/2}$.
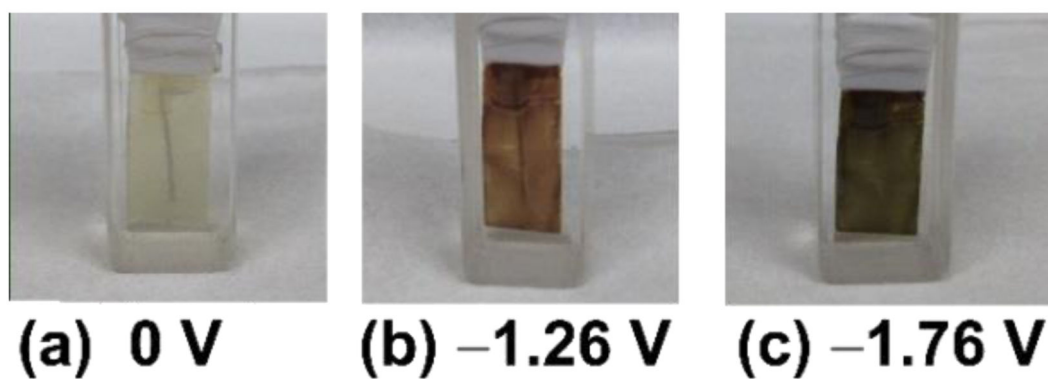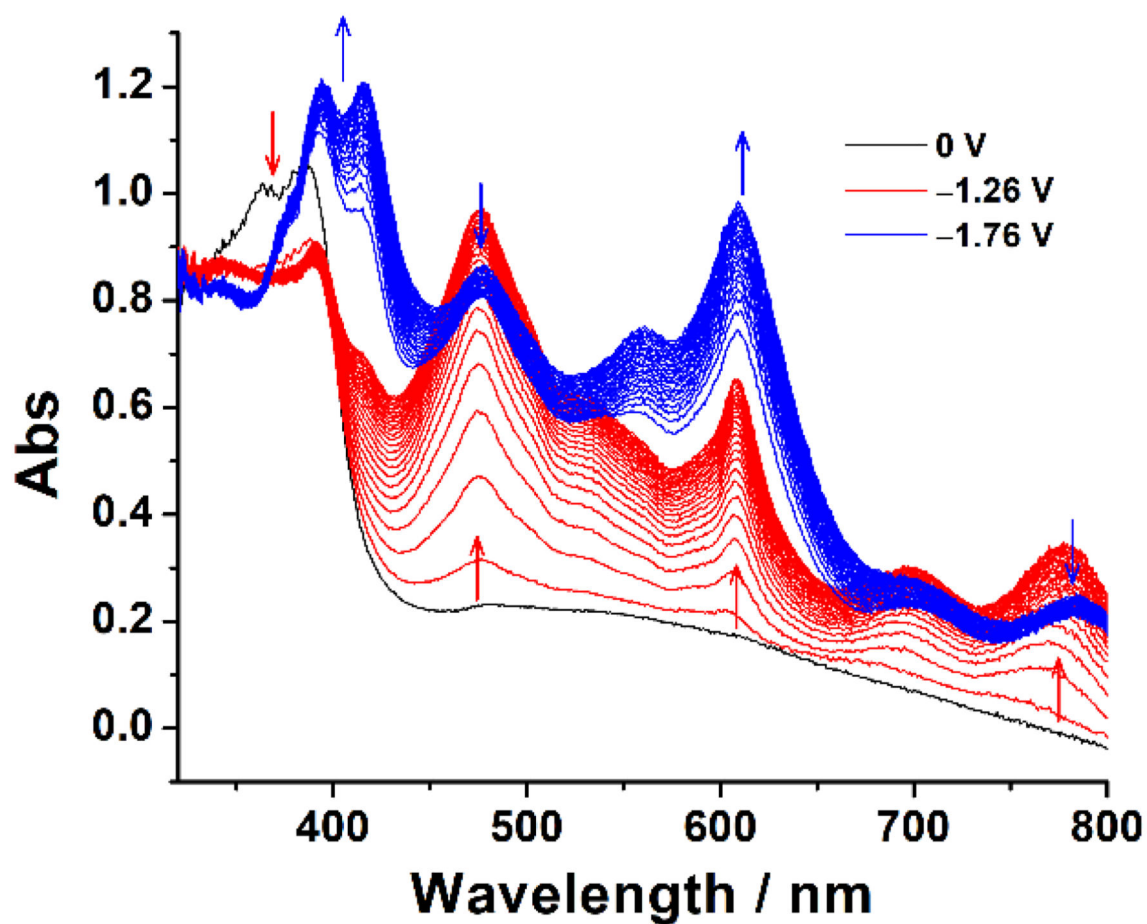
Figure 8.
UV-vis spectroelectrochemical measurements of **Zr(dcphOH-NDI)@FTO** using 0.8 M KPF$_6$/DMF as the supporting electrolyte (top). Photos of **Zr(dcphOH-NDI)@FTO** thin film electrodes (bottom) at various applied potentials (a) 0 V, (b) −1.26 V, and (c) −1.76 V vs. Fc$^{+/0}$

Table 1

Summary of Electrochemical and Optical Properties of Zr(dcphOH-NDI)@FTO thin films

	λ_{max} [nm]	$E_{1/2}^{0/\cdot-}$[V] (E_p [mV])[a]	$E_{1/2}^{\cdot-/2-}$[V] (E_p [mV])[a]
Zr(dcphOH-NDI)@FTO	364, 382	−0.96 (166)	−1.36 (175)
dcphOH-NDI	359, 379	−0.93 (67)	−1.30 (75)

[a]Redox potentials were measured in DMF with 0.8M KPF$_6$ at 50 mV s^{-1}.